1   Revision 1

2   Word Count: 9541 (excluding references)

3   **Electron Probe Microanalysis of Trace Sulfur in Basaltic Glasses and Silicate Minerals**

4   **Anna Johnson[1], Rajdeep Dasgupta[1], Gelu Costin[1], Kyusei Tsuno[1,2]**

5   **Affiliations:** [1]Department of Earth, Environmental and Planetary Sciences, Rice University,

6   6100 Main Street, MS 126, Texas, 77005, USA, [2]Eyring Materials Center, Arizona State

7   University, 1001 S McAllister Avenue, Tempe, Arizona, 85287, USA

8

9   **Abstract**

10   Sulfur (S) in the mantle is conventionally assumed to be exclusively stored in accessory sulfide

11   phases, but recent work shows that the major silicate minerals that comprise >99% of the mantle

12   could be capable of hosting trace amounts of S. Assessing the incorporation of trace S in

13   nominally S-free mantle minerals and determining equilibrium S partitioning between these

14   minerals and basaltic melt requires analyzing small experimental phases with low S contents.

15   Here, we develop a protocol for EPMA analysis of the trace levels of S in silicate phases. We use

16   a suite of natural and experimental basaltic glass primary and secondary standards with S

17   contents ranging from 44 ppm to 1.5 wt.%. The effects of beam current and counting time are

18   assessed by applying currents ranging from 50 to 200 nA and total counting times between 200

19   and 300 seconds at 15 kV accelerating voltage. We find that the combination of 200 nA beam

20   current with a 200 second counting time (80 second peak, 60 seconds each for upper and lower

21   background, respectively) achieves precise yet cost-effective measurements of S down to a

22   calculated detection limit of ~5 ppm and a blank-derived, effective detection limit of ~17 ppm.

23   Close monitoring of the S peak intensity and position throughout the duration of each spot also

24 shows that high currents and extended dwell times do not compromise the accuracy of

25 measurements, and even low S contents of 44 ppm can be reproduced to within one standard

26 deviation. Using our developed recipe, we analyzed a small suite of experimental clinopyroxenes

27 (cpx) and garnets (gt) from assemblages of silicate partial melt + cpx ± gt ± sulfide, generated at

28 1.5 to 3.0 GPa and 1200 to 1300 °C. We find S contents of up to 71 ± 35 ppm in cpx and 63 ± 28

29 ppm in gt, and calculate mineral-melt partition coefficients ($D_s^{min/melt}$) of up to 0.095 ± 0.064 and

30 0.110 ± 0.064 for $D_s^{cpx/melt}$ and $D_s^{gt/melt}$, respectively. The sulfur capacity and mineral-partitioning

31 for cpx are in good agreement with SXRF measurements in a prior study by Callegaro et al.

32 (2020), serving as an independent validation of our EPMA analytical protocol.

33 **Keywords:** Electron probe microanalyzer, sulfur solubility, mantle, silicate glass, clinopyroxene,

34 garnet, partitioning

35

1. Introduction

37 Sulfur (S) is a critical element for planetary differentiation, formation of many ore deposits,

38 chemical habitability of planets, and complex life. Geologists have long sought an accurate

39 understanding of planetary sulfur cycles, particularly as pertaining to S storage in the Earth's

40 mantle (Lorand, 1990; von Gehlen, K. 1992; McDonough and Sun, 1995; Saal et al., 2002;

41 Nielsen et al., 2014; Tsuno and Dasgupta, 2015; Zhang et al., 2016; Ding and Dasgupta, 2017,

42 2018; Sun et al., 2020; Dasgupta et al., 2022), a significant reservoir of volatile storage making

43 up 67% of the planet by mass. This task is complicated by sulfur's volatile nature and by

44 extraction of S-bearing magmas from their sulfide-bearing sources, which obfuscate the pre-

45 melting, sub-solidus source sulfur content. Previous studies have established the concentration of

46 mantle S at a range of values between 100 and 300 ppm (e.g. Nielsen et al., 2014; Ding and

47 Dasgupta, 2017; Sun et al. 2020), based on the assumption that S is hosted exclusively in

48 accessory sulfide phases such as mono-sulfide solid solution (MSS) or mono-sulfide liquid

49 solution (MLS) (Lorand, 1989, 1990; Bockrath et al., 2004; Zhang and Hirschmann, 2016).

50 Recent work, however, has claimed that major silicate mantle minerals—which have thus far

51 been assumed to be S-free—may contain trace amounts of S (Anzures et al., 2019; Callegaro et

52 al., 2014, 2020). Here, we define a trace element as a non-stoichiometric component of a mineral

53 that is present in its crystalline lattice at levels of <0.1 wt.% (1000 ppm). Trace elements may be

54 incorporated into minerals by filling vacancies in the lattice or substituting for elements of

55 similar charges/ionic radii. For example, clinopyroxene has the general formula

56 $(Ca,Mg,Fe,Na)(Mg,Fe,Al)(Si,Al)_2O_6$, but S has been shown to be present at concentrations of up

57 to approximately 50 ppm (Callegaro et all., 2014), hypothetically substituting for bridging

58 oxygen in the M2 cation site (Callegaro et al., 2020). Considering that silicate minerals such as

59 olivine, clinopyroxene, orthopyroxene, garnet, and high-pressure polymorphs of these species

60 comprise >99% of the mantle, the absolute amount of S they could contribute to the estimated

61 bulk Earth S inventory of $\sim 1.8 \times 10^{23}$ kg may be non-negligible, no matter how dilute their

62 concentration within the minerals. Furthermore, not accounting for storage of trace S in

63 nominally sulfur-free minerals may lead to serious underestimation of the bulk mantle S budget.

64 Additionally, incorporation of sulfur into silicate minerals may have an impact on how S is

65 partitioned as the mantle undergoes partial melting or mantle-derived melts undergo

66 differentiation. All current models assume that S is perfectly incompatible after exhaustion of the

67 accessory sulfide phase during mantle melting (e.g. Ding and Dasgupta, 2017; Dasgupta et al.

68 2022) or until sulfide precipitates during magmatic differentiation (e.g. Lee et al., 2012; Ding

69 and Dasgupta, 2017). Comprehensive studies of the sulfur in mantle minerals are, therefore,

70 crucial for better understanding volatile storage and cycling within Earth and other rocky planets.

71   The three prior studies analyzing S in silicate minerals were conducted using secondary

72 ionization mass spectrometry (SIMS) (Anzures et al., 2019) and synchrotron X-ray

73 microfluorescence (SXRF) (Callegaro et al., 2014 and 2020). While both techniques are well-

74 established for the analysis of trace elements, they have the disadvantages of low spatial

75 resolution and high analytical cost/limited availability. In contrast, the electron probe

76 microanalyzer (EPMA), particularly the field emission electron probe microanalyzer (FE-

77 EPMA), offers high spatial resolution with <1 μm^3 analytical volume, which is especially

78 advantageous for fine-grained, polymineralic, and heterogeneous samples. Furthermore, EPMA

79 is more widely available and has significantly lower operational costs.

80   Conventionally, EPMA has been used highly effectively for major and minor element

81 analysis, but at less frequency for trace elements due to numerous challenges presented by the

82 trace realm. For example, trace element analyses require higher beam currents and longer

83 counting times than for routine major element analyses, in order to generate a sufficient quantity

84 of X-rays to resolve the target peak from the background. However, prolonged exposure to high

85 current densities can excessively heat up the irradiated volume and lead to degassing and/or

86 redox change of the target element, which is particularly challenging while analyzing a volatile

87 and multivalent element like sulfur (Hughes et al., 2020). Count precision is directly tied to the

88 accelerating voltage; increased overvoltage allows the beam electrons to penetrate further into

89 the sample, ionizing a greater volume of material but compromising the spatial resolution of the

90 analysis (Reed, 2000; Carpenter and Jolliff, 2015). Trace elements are also more sensitive to

91 various error sources that accompany EPMA analysis, including fluctuation of X-ray emissions,

4

92   incorrect background characterization due to peak interferences, coating effects, calibration

93   effects, and improper matrix correction (Williams et al., 2007). Finally, collection efficiency was

94   a challenge in the past that has now been largely resolved by advances in spectrometer

95   technology (Jercinovic et al., 2012).

96   Despite these difficulties, EPMA-based studies of trace elements have been attempted

97   from as far back as the 1980's (Bodinier et al., 1987, achieving detection limits of titanium down

98   to 5 ppm in orthopyroxene and 4 ppm in olivine), and an increasing volume of work in the past

99   two decades has shown the technique to be capable of highly precise and accurate measurement

100   of trace levels in a range of geologic materials (e.g. Pyle and Spear, 2000; Jercinovic, 2005;

101   Sobolev et al., 2005; Williams et al., 2007; Weiss et al., 2008; Agangi et al., 2015; Korolyuk and

102   Pokhilenko, 2016; Jia et al., 2022; Sørensen et al., 2023). In this study, we develop an EPMA

103   analytical protocol for trace sulfur in silicates, by calibrating the analytical conditions on a series

104   of low-S natural and synthetic glasses. We improve measurement precision by applying a range

105   of high beam currents and counting times to lower detection limits (D.L.) and analytical

106   uncertainty, while checking for any negative irradiation effects and secondary fluorescence. We

107   also assess potential background interferences to characterize the continuum properly for an

108   accurate peak to background ratio that yields correct concentrations, and analyze San Carlos

109   olivine to compare the signal yielded by an assumed blank against the calculated D.L. Finally,

110   we apply the protocol to experimental clinopyroxene and garnet that have been grown in

111   equilibrium with a sulfide phase to ensure maximal uptake of S in the minerals. We validate the

112   recent findings that at shallow upper mantle conditions, non-negligible S may be incorporated

113   into dominant mantle minerals such as clinopyroxene and garnets, with mineral-melt partition

114   coefficients of <0.110.

115

2. Methods

2.1. Standard selection

A series of synthetic and natural basaltic glasses with decreasing S content were selected as

primary and secondary standards with which to optimize analytical conditions for measuring

trace levels of sulfur using FE-EPMA (Table 1). Although our main goal is to analyze silicate

minerals, S-bearing glasses are ideal candidates for assessing the interplay of instrument

conditions, due to uniform distribution of S in homogenous media and the varying concentrations

that can be attained through controlled synthesis. Furthermore, because S concentrations in

silicate minerals have yet to be extensively studied with other methods and no matrix-matched

standards exist yet, basaltic glasses offer the closest major element profile to mafic minerals. For

example, the average atomic number (Z) in our secondary standard FRND6001 is ~16.4,

approaching the typical experimental clinopyroxene average Z of ~15.8 and garnet average Z of

~17.2.

Our primary standard is the Smithsonian standard NMNH 113716-1, a natural basaltic

glass with a documented S content of 1200 ppm (Jarosewich et al., 1980; National Museum of

Natural History, 2019). Because the protocol is developed mainly for sulfide-added samples, we

calibrate the peak position to S^{2-} at approximately 172.072 mm using a natural pyrite (FeS_2)

standard. Synthetic secondary standards G669, B502, B503, and T120 were produced in the Rice

University Experimental Petrology Laboratory (procedure detailed below) as nominally-

anhydrous basaltic glasses doped with 180-1500 ppm S. One natural basalt is also used as a

secondary standard (FRND6001), previously measured as 44 ± 1 ppm using SIMS by Lloyd et

al. (2013).

138

2.2. Sample and standard synthesis

140   **2.2.1. Starting mix.** Synthetic glass standards were produced by mixing the BCR-1

natural basalt standard with sulfur in the form of pulverized natural pyrite to produce a range of

S concentrations: 0.1 wt.% (G669), 0.05 wt.% (B503), 0.02 wt.% (B502), and 0.01 wt.% (T120).

For generating experimental mineral-melt assemblages containing sulfur, we chose a

synthetic basalt composition used in literature and known to yield major upper mantle minerals

clinopyroxene and garnet (Chowdhury and Dasgupta, 2019), and doped the mix with pyrite or

reagent-grade FeS powder to produce low-S (0.10 wt.% S) starting mix HAB1 and high-S (6.08

wt.% S) starting mix HAB2 (Table 2).

148

149   **2.2.2. Experiments.** All experiments were performed using end-loaded piston cylinder

apparatuses at the Rice University Experimental Petrology Laboratory, using half-inch $BaCO_3$

pressure medium and internal crushable MgO spacers to house the sample capsules. An outer Pb

foil was used as lubricant and to contain friable assembly parts. Temperatures were monitored

and controlled using Type-C (W5%Re-W26%Re) thermocouple placed within 1.5 mm of the top

of the samples. The pressure and temperature calibrations of this assembly were given in Tsuno

and Dasgupta (2011) and have been adopted in a number of subsequent studies including several

on the synthesis of S-bearing glasses in equilibrium with sulfide or sulfate (e.g., Ding et al.,

2014, 2018; Chowdhury and Dasgupta, 2019, 2020).

For the synthesis of standard glasses, the starting mix was placed in graphite capsules,

heated to 1600 °C at 100 °C/minute at 1.8 GPa, and were kept for 1 h to produce a homogenous

melt. For the synthesis of experimental mineral-melt assemblages, the starting mix was packed

7

161   into 2 mm deep graphite crucibles with 1.7 mm inner diameter, 3 mm height, and 3.1 mm outer

162   diameter. The graphite crucibles with 1 mm thick circular graphite lids were then loaded into

163   platinum outer capsules, which were subsequently welded shut. Outer platinum capsules were

164   included to minimize physical ingress of volatiles during the experiments, while the inner

165   graphite containers were placed to prevent iron loss to the outer Pt capsule and set the oxygen

166   fugacity to approximately FMQ-1.5 (Medard and Grove, 2008; Bataleva et al., 2018). Five

167   separate experiments were performed at P and T conditions reflective of the shallow upper

168   mantle, at 1.5 GPa/1200 °C (T124, low-S) and 1.5-3.0 GPa/1200-1300 °C (high-S experiments

169   T131, T154, T155, and T168), with run durations of 72 hours. All experiments were pressurized

170   close to the desired target pressures at room temperature and then heated at a rate of

171   100 °C/minute to reach the target experimental temperature. At the end of the desired duration,

172   the samples were rapidly cooled to room temperature by turning off power to the graphite heater

173   and slowly depressurized. Extracted capsules were then cut and polished to expose the resulting

174   phase assemblages (Fig. 1).

175

176   **2.3. Sample preparation and instrument specifications**

177   Trace element analysis requires highly polished sample surfaces, as excessive surface

178   topography and coating deficiencies can lead to charge buildup and fluctuations in absorbed

179   current that introduce significant error in the accuracy of measurements (Jercinovic et al., 2012).

180   Therefore, all standards and samples in this study were polished with progressively higher grit

181   sandpaper, and finally, 0.3 μm alumina slurry on a velvet cloth. The synthesized samples were

182   also impregnated with low viscosity superglue under vacuum prior to polishing, to prevent grain

183   pluck-outs. All standards and samples were then coated with a 25-30 nm thick layer of carbon.

184 Analyses were conducted at the Rice University EPMA laboratory, using a field emission JEOL

185 JXA 8530F Hyperprobe. Voltage was set to 15 kV for all sessions, with a take-off angle of 40°,

186 and a beam diameter of 20 μm for glasses and fully focused spots for minerals. Sulfur was

187 measured on the PETH and PETL crystals, with the S^{2-} peak position calibrated on pyrite and the

188 low and high backgrounds set to -5 mm and +5 mm of the peak. The separate measurements by

189 each crystal, as well as the combination of the two, were compared for reproduction of the

190 primary standard NMNH 113716-1, and PETL was selected as the sole spectrometer for all

191 subsequent analyses due to yielding lower analytical errors and D.L., and reproducing 1200 ppm

192 S to within 1% (Table 3). Major elements were measured concurrently with sulfur (at the same

193 beam current and accelerating voltage) with a 10 second peak counting time and 5 seconds for

194 each background, using TAP (Si, Al, Mg, Na), PETJ (K, Ca), LIFH (Fe), and LIFL (Mn, Ti)

195 crystals. All phases shared jadeite as the standard for Na, rhodonite for Mn, and rutile for Ti. For

196 experimental glasses, the basaltic glass Smithsonian standard NMNH-113716-1 was used for Si,

197 Al, Mg, and Ca, synthetic glass NMNH-117218-3 for K, and olivine for Fe. For experimental

198 clinopyroxenes, diopside was used for Si, Ca, and Mg, olivine for Fe, biotite for K, and

199 plagioclase for Al. Finally, for experimental garnets, almandine was used for Si, Fe, and Al,

200 olivine for Mg, biotite for K, and plagioclase for Ca.

201

202 **3. Results**

203 **3.1. Optimized beam conditions for trace S analysis in silicate materials**

204 In this section we assess varying beam currents and total counting times to identify the

205 combination that produces a clearly resolved peak signal, minimal detection limit, and reduced

206 analytical error. Furthermore, factors that can negatively affect the accuracy of EPMA

9

207   measurements of major and minor elements impart an even greater impact on trace element

208   analyses. Here, we specifically examine the effects of background continuum, matrix

209   corrections, beam damage, and secondary fluorescence on our protocol.

210

211   **3.1.1. Resolution of peak signal.** Successful trace element analysis on EPMA

212   fundamentally depends on the ability to resolve X-ray emissions of a target wavelength (peak)

213   from background emissions. Increased beam current produces more X-ray counts at both the

214   peak and background wavelengths, and improves this resolution, expressed as I_{net} in Equation 1

215   (JEOL, 2020):

216     $$I_{net} = I_{peak} - \frac{I_{PBH}\overline{L_{PBL}} + I_{PBL}\overline{L_{PBH}}}{\overline{L_{PBL}} + \overline{L_{PBH}}}$$ (1)

217   where I_{peak} is the intensity of the peak position (average counts per second/beam current), I_{PBH}

218   and I_{PBL} are the intensity of the backgrounds above and below the peak position, and $\overline{L_{PBL}}$ and

219     $\overline{L_{PBH}}$ are the distances between the peak position and the low and high background positions. In

220   our study, the S Kα position at an L-value of 172.072 mm is bounded by ±5 mm lower and upper

221   offsets of background, at 167.072 mm and 177.072 mm, respectively. Our first-order goal in

222   beam current selection, therefore, was to improve the resolution as expressed by net intensity.

223   Peak scans at 50, 100, 150, and 200 nA (Fig. 2) demonstrated the effect of increased current in

224   improving peak resolution for all standards. Although the improvement is not apparent from

225   Figure 2 for the most dilute glass FRND6001 (44 ppm S), it is important to note that these peak

226   scans were generated by continuously scanning from 171.0 mm to 173.0 mm without dwelling at

227   any point. Therefore, Figure 2 does not capture the extended counting times at peak and

228   background positions that produce resolvable emissions even for concentrations as low as that of

10

229 FRND6001. Background characterization and the peak resolution of FRND6001 are discussed

230 further in section 3.1.3.

231

232 **3.1.2. Detection limit and uncertainty.** Probe current and counting time are critical not

233 only to improving the net intensity, but also to analytical precision as expressed by D.L. and

234 analytical error. The detection limit is calculated as a function of standard and background

235 measurements, with the following equation (JEOL, 2020):

236 $$Detection\ limit\ = \frac{mass(\%)_{STD}}{I_{net\ STD}} \sqrt{\frac{2 \times I_{back}}{t_{back}}} \tag{2}$$

237 where mass(%)$_{STD}$ is the mass concentration of the element of interest in the standard, $I_{net\ STD}$ is

238 its net intensity as measured on the standard, I_{back} is the average intensity of background X-rays,

239 and t_{back} is the total background counting time. The D.L. is lowered by increasing $I_{net\ STD}$ and

240 t_{back}. Given a primary standard with well-established S concentration such as our primary

241 standard Smithsonian glass NMNH 113716-1 (1200 ppm S), increasing the $I_{net\ STD}$ by increasing

242 beam current (as detailed in section 3.1.1) allows the concentration to intensity ratio to be

243 minimized. While each background counting time is typically set to half of the peak dwell time

244 for major element analysis, we extend the background times to 70-75% of the peak time to

245 further lower the D.L. As an added benefit, the longer background dwell times allow for

246 improved background characterization to resolve any interferences that may compromise the

247 accuracy of results (Jercinovic et al., 2012).

248 Counting times and probe current also factor into minimizing analytical uncertainty,

249 calculated as one standard deviation by the following equation (JEOL, 2020):

250 $$S.D.(\%) = \frac{100}{I_{net}} \sqrt{\frac{I_{peak}}{t_{peak}} + \left(\frac{L_{PBH}}{L}\right)^2 \frac{I_{PBL}}{t_{PBL}} + \left(\frac{L_{PBL}}{L}\right)^2 \frac{I_{PBH}}{t_{PBH}}} \tag{3}$$

11

251   where t_{peak} is the peak counting time on the sample, t_{PBH} and t_{PBL} are the counting times at high

252   and low background positions, L is the sum of the background distances, and all other variables

253   are as defined above. As with D.L., we lower the uncertainty by increasing beam current and

254   background counting time, and furthermore increase the peak counting time.

255   To minimize D.L. and uncertainty, as well as compare the effects of beam current and

256   counting times on these parameters, we analyzed our glass standards NMNH-113716-1 (1200

257   ppm S), B503 (599 ppm), T120 (183 ppm), and FRND6001 (44 ppm) at a range of conditions:

258   beam currents of 50, 100, 150, and 200 nA, and total counting times of 200 seconds (80 s

259   peak/60 s per background), 240 seconds (100 s peak/70 s per background), and 300 seconds (120

260   s peak/90 s per background). At these conditions, we observe that the primary control on D.L. is

261   beam current (Fig. 3), approximately halving the limit from 10 ppm to 5 ppm at a total counting

262   time of 200 seconds, while increasing the time to 300 seconds further improves the limit by only

263   <2 ppm. Furthermore, the D.L. at a given set of conditions is identical for all secondary

264   standards, regardless of their S content, since Equation 2 is a function of primary standard

265   concentration and background conditions, and background intensity is roughly constant for any

266   sample at a given beam current (Fig. 2). Analytical uncertainty is also primarily controlled by

267   beam current, displaying a roughly exponential decrease when increasing the current from 50 to

268   200 nA (Fig. 4), while increased counting time for a given beam current only minimally

269   improves the uncertainty, particularly at higher currents. For example, for the primary standard

270   NMNH-113716-1 (1200 ppm S) at 50 nA, increasing dwell time from 200 to 300 seconds

271   improves uncertainty by 0.4%, while the same increase at 200 nA entails a 0.1% improvement

272   (Fig. 4a). Meanwhile, an increase from 50 to 200 nA with a total dwell time of 200 seconds

273   enables a full 1% improvement in analytical uncertainty. This becomes much more significant

12

274   for extremely low sulfur concentrations such as FRND6001 (44 ppm S), with a >50% reduction

275   in error by increasing beam current from 50 to 200 nA at a total counting time of 200 seconds

276   (Fig. 4b), while longer counting times do not necessarily yield lower uncertainty for a given

277   beam current. This is encouraging as shorter dwell times reduce instrument time and accordingly

278   the cost of analysis.

279   To compare the calculated D.L. with how a "blank" signal (i.e. background continuum)

280   may manifest, we apply the optimized beam conditions of 200 nA and 200 s total counting time

281   to measure San Carlos olivine as an analytical blank for sulfur. Although a D.L. as low as 5 ppm

282   is calculated by Equation 2 at these conditions, San Carlos olivine yields an apparent S

283   concentration of 17 ± 5 ppm (Table 3; derived from 49 replicate measurements ranging from <5

284   to 25 ppm, averaging 47 values that exceed the calculated D.L). We consider two possible causes

285   for this non-zero measurement: 1) no sulfur is present (i.e. the olivine is a true "blank"), or the

286   amount present is insufficient to resolve a peak from the background signal, so the value of $17 \pm$

287   5 ppm is an artifact of the background intensity being converted to concentration via matrix

288   correction; 2) the olivine contains trace amounts of sulfur. In the case of 1), regardless of

289   whether the olivine contains S, a peak cannot be resolved and therefore 17 ± 5 ppm should be

290   selected as the D.L. over the calculated value of 5 ppm. On the other hand, the possibility of

291   olivine containing measurable sulfur should also not be easily dismissed. While Callegaro et al.

292   (2020) report a concentration of ≤ 1 ppm S in experimental olivine, Lambart et al. (2022) observe

293   high variability of trace phosphorous in San Carlos olivine that may be attributable to

294   metasomatism. Although sulfur is not investigated in the Lambart et al. (2022) study, it is

295   possible that secondary processes could have produced similar variability, and 17 ± 5 ppm

296   reflects the true sulfur content of the grains available at the Rice University EPMA lab.

13

297   However, lacking systematic and independent verification by a different *in situ* analytical

298   technique, we have decided to consider the San Carlos olivine to be a sulfur "blank" for the

299   purposes of our protocol, and take 17 ± 5 ppm to be the effective D.L. As such, sulfur values

300   reported for all standard reproductions in Table 3 and experimental results in Table 4 are blank-

301   corrected values, from which 17 ppm is subtracted and 5 ppm is propagated through the standard

302   deviation.

303

304   **3.1.3. Peak over background.** Properly characterizing the background signal can be

305   critical to clearly resolving the characteristic X-ray peaks of trace elements from the noise of the

306   continuum. Neglecting subtleties in the background may lead to under- or over-estimating the

307   element of interest, particularly when a peak signal is of lower magnitude than the background

308   (Reed, 2000). Although recent studies have developed sophisticated methods of background

309   analysis (e.g. Allaz et al., 2019), here we focus on directly observing the background and peak

310   counts across the analytical duration (Fig. 5). For glass standard T120 with 180 ppm S, the S Kα

311   peak is distinctly resolved from the -5 mm and +5 mm background signals (Fig. 5a). However,

312   at 44 ppm S (FRND6001, Fig. 5b) the peak is not resolved from the low background at -5 mm,

313   which may be a consequence of overlap with a third-order Fe Kβ_5 peak at approximately 167

314   mm, or simply an effect of spectrometer geometry. To resolve such asymmetries, the JEOL

315   software takes the average of the two backgrounds in the net intensity calculation (Equation 1). If

316   the peak intensity is equal to or less than one of the backgrounds, the net intensity—and by

317   extension, the concentration—will be underestimated. While this compromises the strict

318   accuracy of our measurements at <100 ppm levels, we consider an underestimation to be

319   acceptable as a conservative estimate. Despite this background asymmetry, we find that the

14

320   matrix- and blank-corrected concentration of FRND6001 of 36 ± 13 ppm (Table 3)—taken as an

321   average of 20 points—to be within uncertainty of the literature value of 44 ± 1 ppm as measured

322   by SIMS (Lloyd et al., 2013). All synthetic secondary standards (T120, B502, B503, G669) are

323   also replicated within uncertainty of the S concentrations derived by weighing the experimental

324   starting mixes, while our primary standard NMNH 113716-1 is reproduced to within 1% of the

325   Smithsonian value (Fig. 6).

326

327   **3.1.4. Matrix correction.** The accuracy of trace element analysis also depends heavily on

328   appropriate matrix corrections, which JEOL performs with the Armstrong method PRZ model.

329   Ideally, the primary standard closely matches the composition of the target phase to correct for

330   average atomic number (Z) and absorption (A) as accurately as possible. Although we use a

331   basaltic glass primary standard in this study because S is not present in sufficiently high

332   quantities in a silicate mineral matrix to have an exact match between standard and samples, the

333   average Z of the glass (16.05) closely resembles that of a typical clinopyroxene (16.28), and

334   approaches that of the experimental garnets (19.60). The integrity of the correction could be

335   improved by synthesizing S-rich glasses with major element compositions matching

336   clinopyroxene and garnet, to better account for the contribution of heavily fluorescing, high Z

337   elements like Fe to the overall correction.

338

339   **3.1.5. Beam damage.** The benefits of high beam currents and counting times on the order

340   of hundreds of seconds must be balanced with an increased risk for beam damage. Exposing a

341   sample to high current densities for extended periods heats the target area and can lead to factors

342   such as volatile loss and redox change of Fe and S in glasses (Hughes et al., 2020). Both

343 phenomena may lead to underestimation of the S concentration in samples, the former through

344 loss of material, and the latter by not all X-ray emissions being collected when the peak position

345 has changed from the specified L-value (the S^{6+} of anhydrite is typically located at

346 approximately -0.1 mm with respect to S^{2-}). We address these concerns by verifying the stability

347 of the S Kα counts and the peak L-value over time.

348   First, we recorded the intensity of S Kα X-ray emissions (counts per second) and

349 absorbed current (nA) throughout the dwell time on each glass standard at varying currents, to

350 assess whether our analytical conditions cause a progressive drop in S Kα peak counts that would

351 suggest devolatilization by beam damage. Even at the highest current of 200 nA, the count rate

352 remains constant throughout the peak and each of the backgrounds, as indicated by the flat trend

353 in intensity fluctuations and absorbed current recorded on the 180 ppm standard T120 (Fig. 5a)

354 and the 44 ppm standard FRND60 (Fig. 5b). From this, we conclude that devolatilization of S is

355 not a concern with the selected conditions.

356   Although the stable count intensity may be sufficient to suggest that redox change is not

357 occurring to any significant extent, we also monitored the peak position against elapsed time for

358 any shift to a lower L-value that would indicate beam-induced oxidation. We tested for peak shift

359 by applying a 15 kV, 200 nA beam with 20 μm spot size to the Smithsonian standard glass

360 NMNH 113716-1 and running a peak scan twice on a single designated point. This particular test

361 was conducted during a different analytical session from the preceding tests, and the S^{2-} peak

362 position calibrated on pyrite was 172.122 mm instead of the aforementioned 172.072 mm. The

363 duration of each peak scan was 400 seconds total across the L-value range of 171.1 to 173.1 mm

364 (10 μm steps, 2000 ms per step). Approximately 1/3 of the total time, or 130 seconds of each

365 scan is spent on the peak area, allowing a high-resolution view of the effects of prolonged beam

16

366   exposure. On the first scan, a single peak is seen at 172.065 mm (Fig. 7a), suggesting the sulfur

367   in NMNH 113716-1 is in some intermediate redox state, more oxidized than pyrite. On the

368   second scan, after >260 seconds spent irradiating the same spot, the morphology of the peak has

369   changed slightly but the central peak position remains the same (Fig. 7b). We conclude that no

370   notable redox change has occurred as a result of irradiation. Furthermore, the native Peak Scan

371   functionality of JEOL software accounts for any variability of peak position to within ±1 mm of

372   the calibrated position, scanning for the spot-specific peak position within this range prior to

373   beginning the dwell time.

374

375   **3.1.6. Secondary fluorescence.** In contrast to beam damage, which can lead to

376   underestimation of mobile cations and volatile elements, secondary fluorescence can cause

377   concentrations to be overestimated. Secondary fluorescence is a phenomenon in which

378   characteristic and continuum X-rays interact with neighboring phases that contain the target

379   element to generate secondary signals of that element (Reed and Long, 1963; Gavrilenko et al.,

380   2023). Given that abundant sulfides are distributed throughout the fine-grained textures of our

381   high-S experiments (Fig. 1b), the potential effects of this phenomenon need to be carefully

382   assessed. We used the Monte Carlo program PENEPMA (Llovet and Salvat, 2017) to model the

383   secondary fluorescence of S in diopside from neighboring pyrrhotite, and find that at 1 μm from

384   the boundary with a sulfide, secondary fluorescence accounts for approximately 0.17% of the K-

385   ratio of the S measurement; this decreases to 0.017% at a distance of 10 μm and 0.004% at 20

386   μm. Based on these results, we can minimize the effects of any secondary fluorescence by

387   selecting mineral grains at least 20 μm in diameter and placing spots >10 μm away from

388   neighboring sulfides—where visible at the surface—and calculating the final S concentration of

389   grains in a specific experiment by taking the average of 20 spot analyses in the target silicate

390   phases.

391

392   **3.2. Experimental results**

393   **3.2.1. Textures and phase assemblages of standards and samples.** All synthesized

394   standards have a homogenous glassy texture, lacking any zoning and sulfide phases identifiable

395   in backscattered electron (BSE) images. Natural standard FRND6001 is glassy with some <100

396   µm grains of orthopyroxene and plagioclase that were avoided when setting analytical spots. The

397   low-S experiment T124 (1.5 GPa/1200 °C) yielded an assemblage of silicate partial melt and

398   clinopyroxene. The clinopyroxenes are situated against the capsule wall in an aggregation of <10

399   µm diameter grains with minimal zoning visible in BSE images (Fig. 1a). One high-S

400   experiment, T131 (1.5 GPa/1200 °C), yielded a nearly identical assemblage of silicate partial

401   melt and clinopyroxene, with the addition <20 µm sulfide blebs densely scattered throughout the

402   sample. The remaining high-S experiments T154 (2.5 GPa/1250 °C), T155 (3.0 GPa/1250 °C),

403   and T168 (3.0 GPa/1300 °C; Fig. 1b) all yielded an assemblage of silicate partial melt,

404   clinopyroxene, garnet, and sulfide melt. Garnet and clinopyroxene were present as two

405   interconnected layers at the bottom or cooler end of the capsule (Fig. 1b), with garnet

406   dodecahedrons measuring 5 to 30 µm in diameter, and subhedral clinopyroxene grains with

407   dimensions of <50 µm. Some zoning and clinopyroxene inclusions are visible in the garnets.

408   Sulfide blebs are scattered throughout the experimental samples, and increase in size and

409   decrease in number with increasing temperature.

410

411   **3.2.2. Mineral and melt compositions from phase equilibria experiments.** Table 4

412   provides the major element and S compositions of the experimental phases. Experimental glasses

413   range from basalt to basaltic-andesite with SiO_2 in the range of ~52-58 wt.% and total alkalis

414    $(Na_2O + K_2O)$ of 2-3 wt.%, and FeO^T ranges from ~4 to 9 wt.%. Experimental clinopyroxenes in

415   T124, T131, T154, and T155 are classified as augite to diopside, with 44-49% Wo, 34-44% En,

416   and 13-17% Fs. Clinopyroxene in T168 classifies as pigeonite, with an increased Al_2O_3 content

417   (~14 wt.%) reducing the cation proportion of Ca to 12% Wo. Garnets in T131 and T154 trend

418   toward almandine-rich compositions with 38-39% Alm, 30-35% Prp, and 28-31% Grs, while

419   garnet in T155 is pyrope-rich with 22% Alm, 48% Prp, and 29% Grs.

420

421   **3.2.3. Application of EPMA for S analysis in nominally S-free, experimental silicate**

422   **minerals.** Having established that glass standards with S as dilute as 44 ppm are reproducible

423   within acceptable uncertainty and an effective D.L. of 17 ± 5 ppm can be achieved using EPMA

424   with optimized analytical conditions of 15 kV accelerating voltage, 200 nA beam current, and

425   200 s total counting time, here we test our protocol by analyzing S in experimental silicate

426   phases. Given the scarcity of data in existing literature, our aim for the analytical protocol is to

427   produce measurements that can establish the order of magnitude of S in minerals, at a minimum,

428   with further room for improvement in the future.

429   For the sulfide-undersaturated sample with low bulk sulfur content (T124), we analyzed

430   silicate melt and coexisting clinopyroxenes. The glass S content measures 802 ± 20 ppm sulfur,

431   with all spot analyses exceeding the D.L. and no anomalously high measurements (Table 4).

432   Considering the 0.1 wt.% bulk S content of the starting mix and expected concentration within

433   the melt phase through the growth of nominally S-free crystals, the reduced S content suggests

434 some sulfur has escaped from the capsule, likely during initial heating of the experiment. Of the

435 20 replicate analyses of the experimental clinopyroxene, 13 spots yield S values below the

436 effective D.L. of 17 ppm, while three spots yield anomalously high sulfur contents of hundreds

437 ppm, suggesting the analytical volume may have incorporated a melt zone or small quench

438 sulfide that was not visible when setting points on the surface of the sample (Fig. 8). Discarding

439 these datapoints, the four viable measurements yield an average S of 62 ± 24 ppm in

440 clinopyroxene. Given the point to point heterogeneity, and upward bias introduced by discarding

441 points below the D.L., we take this as an upper bound of S in clinopyroxene in this experiment.

442   For the high-S bulk composition, due to the abundance of sulfides in the experimental

443 assemblage, analyses with anomalously high S values were excluded as they may reflect

444 contamination from tiny sulfide globules present below the sample surface, within the excitation

445 volume of analyses. As reported in Table 4, S contents of our sulfide-saturated experimental

446 glasses (T131, T154, T155, T168) range from 447 ± 189 to 775 ± 71 ppm. Unlike with sulfide-

447 undersaturated T124, all sulfur analyses in minerals exceed the D.L. Clinopyroxene S contents

448 range from 38 ± 17 to 71 ± 35 ppm, and garnets range from 47 ± 28 to 63 ± 28 ppm. To our

449 knowledge, this is the first sulfur content determination of garnet from a sulfide-bearing

450 experimental assemblage.

451

452   **4. Discussion**

453 **4.1. Approach to equilibrium**

454 Our high-S experiments are conducted at sulfide saturation to allow maximum uptake of sulfur

455 by the coexisting silicate minerals and melt, thereby establishing the S content at sulfide

456 saturation (SCSS) or S capacity of the minerals as well as the melt. Before discussing mineral S

457   analyses, however, it is critical to assess how closely our experiments approached equilibrium.

458   Approach to equilibrium for the four reported experiments can be established by the following

459   criteria. First, our experiments were run for approximately 72 h, which is comparable to or

460   exceeds previous experimental durations employed for melt SCSS determination at similar

461   temperatures (e.g., Ding et al., 2014, 2018). Second, to our knowledge, sulfur diffusivity in

462   nominally S-free minerals is undetermined. However, application of a sulfur diffusivity model

463   for S^{2-} diffusion in hydrous basaltic to andesitic melt at sulfide saturation (Freda et al., 2005), at

464   our experimental conditions, yields values from 2.3×10^{-11} m^2/s to 4.9×10^{-11} m^2/s. The application

465   of this diffusivity range suggests that S would diffuse ~3-5 mm through melts during our

466   experiments. Given that sulfide blebs are spaced throughout the melt pool and mineral layers at

467   intervals of <50 μm, the entire melt volume in our experiments are expected to be equilibrated

468   with the sulfide phase. Third, the melt S content of our sulfide-saturated experiments is in good

469   agreement with SCSS values calculated for the relevant conditions with the Smythe et al. (2017)

470   model (using PySulfSat, Wieser and Gleeson, 2023, overlapping within one standard deviation

471   of calculated values (e.g. 775 ± 71 ppm observed, compared to 740 ± 202 ppm calculated, for

472   T131; Table 4), suggesting our experiments closely approached equilibration with respect to melt

473   sulfide capacities.

474

475   **4.2. Comparison with previous studies**

476   To assess the validity of our EPMA measurements of sulfur in nominally S-free, experimental

477   silicate minerals, we compare both the absolute S content in silicate minerals and calculated

478   mineral-melt partition coefficients ($D_s^{min/melt}$) with the SXRF results of Callegaro et al. (2020).

479   For the most apt comparison, we select from Callegaro et al. (2020) two sulfide-saturated and

480   four sulfide-undersaturated experiments, all bearing clinopyroxene and run at reduced conditions

481   with a basaltic starting mix, equilibrated at 0.8-1.0 GPa and 1000-1240 °C. The S content of

482   clinopyroxene in the sulfide-saturated experiments are reported as 38 ± 11 ppm and 54 ± 22 ppm

483   (Callegaro et al., 2020), of which all clinopyroxenes and garnets in our sulfide-saturated

484   experiments are within error (Fig. 9). From this, our results agree that the SCSS of clinopyroxene

485   is on the order of 10^1 ppm. Additionally, consistency between the SXRF results and our sulfide-

486   rich, high-S charges suggests that the EPMA-specific concern of secondary fluorescence does

487   not have a notable effect when measuring trace levels of sulfur in sulfide-saturated experimental

488   assemblages, provided that points are placed at least 10 µm away from any visible sulfides. At

489   sulfide-undersaturated conditions, Callegaro et al. (2020) record clinopyroxene S contents of 25

490   ± 11 to 31 ± 9 ppm, which are lower than those at sulfide saturation, albeit with some

491   overlapping range when uncertainty is considered. In contrast, the S content of our sulfide-

492   undersaturated clinopyroxene is fully within range of the sulfide-saturated minerals, at $<62 \pm 24$

493   ppm. We emphasize that this value is an upper limit that likely reflects an upward skew in the

494   averaging of replicate measurements, an artifact of most measurements falling below the D.L

495   (Fig. 8). The effects of heterogeneity among the replicate measurements are discussed in further

496   detail below.

497   In addition to the absolute S of minerals, we also compare the $D_s^{min/melt}$ between the two

498   studies, calculated as follows:

499    $$D_s^{min/melt} = \frac{[S]_{min}}{[S]_{melt}} = \frac{SCSS_{min}}{SCSS_{melt}} \qquad (4)$$

500   where $[S]_{min}$ is the mineral S content and $[S]_{melt}$ is the melt S, respectively interchangeable with

501    $SCSS_{min}$ and $SCSS_{melt}$ in sulfide-saturated experiments. For sulfide-free T124, our experimental

502    $D_s^{cpx/melt}$ is calculated as $<0.077 \pm 0.030$. For our sulfide-saturated experiments, $D_s^{cpx/melt}$ ranges

22

503   from 0.052 ± 0.025 to 0.095 ± 0.064 and $D_s^{gt/melt}$ ranges from 0.075 ± 0.045 to 0.110 ± 0.064.

504   The sulfide-saturated $D_s^{min/melt}$ are within error of the corresponding Callegaro et al. (2020)

505   partition coefficients of 0.069 ± 0.027 and 0.075 ± 0.034 (Fig. 9). At sulfide undersaturation, the

506   Callegaro et al. (2020) partition coefficients range from 0.023 ± 0.010 to 0.028 ± 0.008, lower

507   than our maximum sulfide-undersaturated $D_s^{cpx/melt}$ by over a standard deviation. However, again

508   we emphasize that the $[S]_{min}$ here is an upper limit, and a lower $D_s^{cpx/melt}$ within range of the

509   Callegaro et al. (2020) values would likely be obtained if the majority of S measurements could

510   be resolved below the effective D.L. of 17 ppm. These broadly consistent results suggest that at

511   crustal and upper mantle conditions, S is incompatible in silicate minerals with partition

512   coefficients on the order of 10^{-2} to 10^{-1}.

513   As reflected in the large standard deviations of the mean $SCSS_{min}$ and $D_s^{min/melt}$ values, the

514   sulfur content of minerals display considerable heterogeneity from spot to spot. In the case of the

515   low-S run, this results in 65% of the mineral spot analyses falling below the effective D.L. (Fig.

516   8), skewing the mean $SCSS_{min}$ and $D_s^{min/melt}$ toward a higher value due to omission of these

517   datapoints. Conversely, the sulfide-saturated experiments yielded some high outliers (e.g. >300

518   ppm) which were discarded from the mean calculations. Such heterogeneity may be caused by

519   incomplete equilibration in terms of sulfur in the low-S experiment, or inclusion of subsurface

520   sulfides in the excitation volume of EPMA analyses in the high-S experiments. Alternatively, or

521   in combination with these two causes, another factor may be nanoscale inclusions of sulfides

522   within the silicate mineral matrix, a phenomenon observed in the natural world with sulfides in

523   diamonds (Logvinova et al., 2010) and platinum group element-rich nanocrystals in sulfides

524   (Wirth et al., 2013). If the observed S is hosted in such nanoinclusions rather than or in addition

525   to being structurally bound, heterogeneity of the measurements may by correlated to the

23

526   distribution of the nanoinclusions, with a higher modal abundance and density of sulfides

527   increasing the probability of these being captured in the e-beam excitation volume. Although the

528   EPMA beam can be focused down to <0.1 μm, the resolution of the BSE image at our imaging

529   conditions is limited to the effective beam size of 300-350 nm; any resolvable inclusions exposed

530   at the surface are avoided when setting the spot, but smaller features and subsurface inclusions

531   cannot be avoided. Similarly, the SXRF measurements by Callegaro et al. (2020) were focused

532   to 6 × 6 μm, and it is unknown whether element mapping was used to assess the homogeneity of

533   the targeted region. However, the authors do note that the natural diopside and clinopyroxene

534   standards used for the SXRF analyses display heterogeneous S concentrations. Given that the S

535   content of these standards were determined by bulk analysis (each containing 32 ppm), it is

536   entirely possible the sulfur is hosted primarily in nanoinclusions that manifest as heterogeneity in

537   spot analysis. Considering the heterogeneity of analyses and the bias toward higher values in the

538   low-S experiment, we consider the $[S]_{min}$ and possibly even $SCSS_{min}$ as well as corresponding

539    $D_s^{min/melt}$ to be maximum values that place an upper limit on sulfur incorporation in nominally S-

540   free silicate minerals. Further analyses should be conducted with a higher sensitivity technique

541   such as NanoSIMS to assess for nanoinclusions and eliminate any effects of heterogeneity to

542   measure the true concentration of structurally-bound sulfur. Furthermore, if NanoSIMS confirms

543   the presence of sulfide nanoinclusions in silicate minerals at reduced oxygen fugacity conditions,

544   then this would: 1) question the interpretation of Callegaro et al. (2020) regarding S^{2-} replacing

545   bridging oxygen in the clinopyroxene lattice; and 2) require a correction to silicate mineral-melt

546   partition coefficients of sulfur. Transmission Electron Microscope (TEM) investigation may also

547   reveal any possible nanoinclusions of sulfides in silicate mineral phases. In summary, although

548   electron microprobe analysis of trace sulfur is challenging, our developed EPMA protocol will

24

549 allow S analyses down to ~ 17 ppm if structurally-bound S in minerals reach that level of

550 concentration.

551

5. Conclusions and Implications

553 We have developed a method of analyzing sulfur in silicate minerals using EPMA, by calibrating

554 optimum probe current and counting time with a series of low-S, natural and synthetic glasses.

555 We find that with a beam current of 200 nA, peak counting time of 80 seconds, and background

556 counting time of 60 seconds (200 second total counting time), we achieve a theoretical D.L. of 5

557 ppm and olivine "blank"-based effective D.L. of 17 ± 5 ppm, with analytical uncertainty of

558 approximately 11-14%. These beam conditions are capable of reproducing the concentration of a

559 44 ppm S glass (measured using SIMS) to within one standard deviation at 36 ± 13 ppm. Using

560 these optimized analytical conditions, we measure the S content of nominally S-free minerals in

561 experimentally synthesized assemblages of clinopyroxene + glass and clinopyroxene + glass +

562 sulfide ± garnet, reporting glass S of 447 ± 189 to 802 ± 20 ppm, clinopyroxene S of 38 ± 17 to

563 71 ± 35 ppm, and garnet S of 47 ± 28 to 63 ± 28 ppm. We also calculate mineral-melt partition

564 coefficients ranging from 0.052 ± 0.025 to 0.095 ± 0.064 for $D_s^{cpx/melt}$ and 0.075 ± 0.045 to 0.110

565 ± 0.064 for $D_s^{gt/melt}$. Although the clinopyroxene S content and $D_s^{cpx/melt}$ of our sulfide-

566 undersaturated experiment T124 falls within the range of the sulfide-saturated counterparts, we

567 consider the sulfide-free values to be strictly an upper bound due to the limited number of viable

568 measurements, and anticipate the true value to be considerably lower if values below the D.L.

569 could be resolved. The clinopyroxene SCSS values closely resemble prior SXRF analyses by

570 Callegaro et al. (2020) experimental clinopyroxenes produced under similar conditions,

571 apparently confirming their results and validating our technique, with the potential to

25

572 significantly affect our understanding of sulfur storage in the mantle. High heterogeneity is noted

573 in the silicate mineral S contents, which we hypothesize may be caused by insufficient diffusion

574 of S, sulfide nanoinclusions, or some combination of the two factors. Because such nanoscale

575 heterogeneities are not resolvable by EPMA or SXRF, we recommend that the reported storage

576 capacity and partition coefficients are considered to be maximum values that may not necessarily

577 reflect the presence of S by trace element substitution in silicate mineral lattices. Further work by

578 NanoSIMS may provide better and complementary information on structurally-bound S

579 concentration in nominally S-free minerals. Despite these sample-related challenges for silicate

580 mineral analysis, we consider our protocol to be a robust and accessible method for the analysis

581 of trace S in homogenous silicate phases with 10's of ppm S.

582

588

589 **References**

590 Agangi, A., Przybyłowicz, W., and Hofmann, A. (2015) Trace element mapping of pyrite from

591 Archean gold deposits – A comparison between PIXE and EPMA. Nuclear Instruments

592 and Methods in Physics Research Section B: Beam Interactions with Materials and

593 Atoms, 348, 302–306.

594   Allaz, J.M., Williams, M.L., Jercinovic, M.J., Goemann, K., and Donovan, J. (2019) Multipoint

595   Background Analysis: Gaining Precision and Accuracy in Microprobe Trace Element

596   Analysis. Microscopy and Microanalysis, 25, 30–46.

597   Anzures, B.A., Parman, S.W., Boesenber, J.S., and Milliken, R.E. (2019) Using Volatile (S, C,

598   H, F, Cl) Contents of Enstatite in Reduced Meteorites to Estimate Oxygen Fugacity and

599   Equilibrium Melt Compositions: LPI Contributions no. 2132.

600   Bataleva, Y., Palyanov, Y., and Borzdov, Y. (2018) Sulfide Formation as a Result of Sulfate

601   Subduction into Silicate Mantle (Experimental Modeling under High P,T-Parameters).

602   Minerals, 8, 373.

603   Bockrath, C., Ballhaus, C., and Holzheid, A. (2004) Fractionation of the Platinum-Group

604   Elements During Mantle Melting. Science, 305, 1951–1953.

605   Bodinier, J.-L., Dupuy, C., Dostal, J., and Merlet, C. (1987) Distribution of trace transition

606   elements in olivine and pyroxenes from ultramafic xenoliths; application of microprobe

607   analysis. American Mineralogist, 72, 902–913.

608   Callegaro, S., Baker, D.R., De Min, A., Marzoli, A., Geraki, K., Bertrand, H., Viti, C., and

609   Nestola, F. (2014) Microanalyses link sulfur from large igneous provinces and Mesozoic

610   mass extinctions. Geology, 42, 895–898.

611   Callegaro, S., Geraki, K., Marzoli, A., De Min, A., Maneta, V., and Baker, D.R. (2020) The

612   quintet completed: The partitioning of sulfur between nominally volatile-free minerals

613   and silicate melts. American Mineralogist, 105, 697–707.

614   Carpenter, P.K., and Jolliff, B.L. (2015) Improvements in EPMA: Spatial Resolution and

615   Analytical Accuracy. Microscopy and Microanalysis, 21, 1443–1444.

616   Chowdhury, P., and Dasgupta, R. (2019) Effect of sulfate on the basaltic liquidus and sulfur

617   Concentration at Anhydrite Saturation (SCAS) of hydrous basalts–Implications for sulfur

618   cycle in subduction zones. Chemical Geology, 522, 162–174.

619   Chowdhury, P., and Dasgupta, R. (2020) Sulfur extraction via carbonated melts from sulfide-

620   bearing mantle lithologies – Implications for deep sulfur cycle and mantle redox.

621   Geochimica et Cosmochimica Acta, 269, 376–397.

622   Dasgupta, R., Chowdhury, P., Eguchi, J., Sun, C., and Saha, S. (2022) Volatile-bearing Partial

623   Melts in the Lithospheric and Sub-Lithospheric Mantle on Earth and Other Rocky

624   Planets. Reviews in Mineralogy and Geochemistry, 87, 575–606.

625   Ding, S., Dasgupta, R., and Tsuno, K. (2014) Sulfur concentration of martian basalts at sulfide

626   saturation at high pressures and temperatures – Implications for deep sulfur cycle on

627   Mars. Geochimica et Cosmochimica Acta, 131, 227–246.

628   Ding, S., and Dasgupta, R. (2017) The fate of sulfide during decompression melting of peridotite

629   – implications for sulfur inventory of the MORB-source depleted upper mantle. Earth and

630   Planetary Science Letters, 459, 183–195.

631   Ding, S., Hough, T., and Dasgupta, R. (2018) New high pressure experiments on sulfide

632   saturation of high-FeO∗ basalts with variable TiO2 contents – Implications for the sulfur

633   inventory of the lunar interior. Geochimica et Cosmochimica Acta, 222, 319–339.

634   Freda, C., Baker, D.R., and Scarlato, P. (2005) Sulfur diffusion in basaltic melts. Geochimica et

635   Cosmochimica Acta, 69, 5061–5069.

636   Gavrilenko, M., Batanova, V.G., Llovet, X., Krasheninnikov, S., Koshlyakova, A.N., and

637   Sobolev, A.V. (2023) Secondary fluorescence effect quantification of EPMA analyses of

638   olivine grains embedded in basaltic glass. Chemical Geology, 621, 121328.

639   Hughes, E.C., Buse, B., Kearns, S.L., Brooker, R.A., Di Genova, D., Kilgour, G., Mader, H.M.,

640   and Blundy, J.D. (2020) The microanalysis of iron and sulphur oxidation states in silicate

641   glass–- Understanding the effects of beam damage. IOP Conference Series: Materials

642   Science and Engineering, 891, 012014.

643   Jarosewich, E., Nelen, J.A., and Norberg, J.A. (1980) Reference Samples for Electron

644   Microprobe Analysis*. Geostandards and Geoanalytical Research, 4, 43–47.

645   JEOL (2020) EPMA Application Software manual [Online]. Available:

646   https://web.gps.caltech.edu/facilities/analytical/microprobe/JEOL_EPMA_software.pdf

647   [accessed May 2023].

648   Jercinovic, M.J. (2005) Analytical perils (and progress) in electron microprobe trace element

649   analysis applied to geochronology: Background acquisition, interferences, and beam

650   irradiation effects. American Mineralogist, 90, 526–546.

651   Jercinovic, M.J., Williams, M.L., Allaz, J., and Donovan, J.J. (2012) Trace analysis in EPMA.

652   IOP Conference Series: Materials Science and Engineering, 32, 012012.

653   Jia, L.-H., Mao, Q., Tian, H.-C., Li, L.-X., Qi, L., Wu, S.-T., Yuan, J.-Y., Huang, L.-L., and

654   Chen, Y. (2022) High-precision EPMA measurement of trace elements in ilmenite and

655   reference material development. Journal of Analytical Atomic Spectrometry, 37, 2351–

656   2361.

657   Korolyuk, V.N., and Pokhilenko, L.N. (2016) Electron probe determination of trace elements in

658   olivine: thermometry of depleted peridotites. Russian Geology and Geophysics, 57,

659   1750–1758.

660   Lambart, S., Hamilton, S., and Lang, O.I. (2022) Compositional variability of San Carlos olivine.

661   Chemical Geology, 605, 120968.

29

662   Lee, C.-T.A., Luffi, P., Chin, E.J., Bouchet, R., Dasgupta, R., Morton, D.M., Le Roux, V., Yin,

663   Q., and Jin, D. (2012) Copper Systematics in Arc Magmas and Implications for Crust-

664   Mantle Differentiation. Science, 336, 64–68.

665   Li, C., and Ripley, E.M. (2009) Sulfur Contents at Sulfide-Liquid or Anhydrite Saturation in

666   Silicate Melts: Empirical Equations and Example Applications. Economic Geology, 104,

667   405–412.

668   Llovet, X., and Salvat, F. (2017) PENEPMA: A Monte Carlo Program for the Simulation of X-

669   Ray Emission in Electron Probe Microanalysis. Microscopy and Microanalysis, 23, 634–

670   646.

671   Lloyd, A.S., Plank, T., Ruprecht, P., Hauri, E.H., and Rose, W. (2013) Volatile loss from melt

672   inclusions in pyroclasts of differing sizes. Contributions to Mineralogy and Petrology,

673   165, 129–153.

674   Logvinova, A.M., Wirth, R., and Sobolev, N.V. (2010) Fluid/melt inclusions in alluvial

675   Northeast Siberian diamonds: new approach on diamond formation: Abstract EGU2010-

676   1236 presented at 2010 EGU General Assembly, Vienna, Austria, 2-7 May.

677   Lorand, J.P. (1989) Abundance and distribution of Cu-Fe-Ni sulfides, sulfur, copper and

678   platinum-group elements in orogenic-type spinel lherzolite massifs of Arirge

679   (northeastern Pyrenees, France). Earth and Planetary Science Letters, 93, 50–64.

680   Lorand, J.P. (1990) Are spinel Iherzolite xenoliths representative of the abundance of sulfur in

681   the upper mantle? Geochimica et Cosmochimica Acta, 54, 1487–1492.

682   Mavrogenes, J.A., and O'Neill, H.St.C. (1999) The relative effects of pressure, temperature and

683   oxygen fugacity on the solubility of sulfide in mafic magmas. Geochimica et

684   Cosmochimica Acta, 63, 1173–1180.

685 McDonough, W.F., and Sun, S.-s. (1995) The composition of the Earth. Chemical Geology, 120,

686   223–253.

687 Médard, E., and Grove, T.L. (2008) The effect of H2O on the olivine liquidus of basaltic melts:

688   experiments and thermodynamic models. Contributions to Mineralogy and Petrology,

689   155, 417–432.

690 National Museum of Natural History (2019) Smithsonian Microbeam Standards Datasheets

691   [Online]. Available: https://naturalhistory.si.edu/research/mineral-sciences/collections-

692   overview/reference-materials/smithsonian-microbeam-standards [accessed November,

693   2023].

694 Nielsen, S.G., Shimizu, N., Lee, C.-T.A., and Behn, M.D. (2014) Chalcophile behavior of

695   thallium during MORB melting and implications for the sulfur content of the mantle.

696   Geochemistry, Geophysics, Geosystems, 15, 4905–4919.

697 Pyle, J.M., and Spear, F.S. (2000) An empirical garnet (YAG) – xenotime thermometer.

698   Contributions to Mineralogy and Petrology, 138, 51–58.

699 Reed, S.J.B., and Long, J.V.P. (1963) Electron-Probe Measurements near Phase Boundaries. In

700   H.H. Pattee, V.E. Cosslett, and A. Engström, Eds., X-ray Optics and X-ray Microanalysis

701   pp. 317–327. Academic Press.

702 Reed, S.J.B. (2000) Quantitative Trace Analysis by Wavelength-Dispersive EPMA.

703   Mikrochimica Acta, 132, 145–151.

704 Saal, A.E., Hauri, E.H., Langmuir, C.H., and Perfit, M.R. (2002) Vapour undersaturation in

705   primitive mid-ocean-ridge basalt and the volatile content of Earth's upper mantle. Nature,

706   419, 451–455.

707   Smythe, D.J., Wood, B.J., and Kiseeva, E.S. (2017) The S content of silicate melts at sulfide

708   saturation: New experiments and a model incorporating the effects of sulfide

709   composition. American Mineralogist, 102, 795–803.

710   Sobolev, A.V., Hofmann, A.W., Sobolev, S.V., and Nikogosian, I.K. (2005) An olivine-free

711   mantle source of Hawaiian shield basalts. Nature, 434, 590–597.

712   Sørensen, B.E., Ryan, E.J., Larsen, R., Lode, S., Røstad, J., and Grant, T.B. (2023) Planar

713   features, Trace element32obilizationn and recrystallization formed during lower crustal

714   CO2 induced seismic deformation of olivine. Abstract EGU23-13208 presented at 2023

715   EGU General Assembly, Vienna, Austria, 23-28 April.

716   Sun, Z., Xiong, X., Wang, J., Liu, X., Li, L., Ruan, M., Zhang, L., and Takahashi, E. (2020)

717   Sulfur abundance and heterogeneity in the MORB mantle estimated by copper

718   partitioning and sulfur solubility modelling. Earth and Planetary Science Letters, 538,

719   116169.

720   Tsuno, K., and Dasgupta, R. (2011) Melting phase relation of nominally anhydrous, carbonated

721   pelitic-eclogite at 2.5–3.0 GPa and deep cycling of sedimentary carbon. Contributions to

722   Mineralogy and Petrology, 161, 743–763.

723   Tsuno, K., and Dasgupta, R. (2015) Fe–Ni–Cu–C–S phase relations at high pressures and

724   temperatures – The role of sulfur in carbon storage and diamond stability at mid- to deep-

725   upper mantle. Earth and Planetary Science Letters, 412, 132–142.

726   Von Gehlen, K. (1992) Sulfur in the Earth's Mantle – A Review. In Schidlowski, M, Golubic,

727   S., Kimberley, M. M., McKirdy, D. M., and Trudinger, P. A., Eds., Early Organic

728   Evolution, p. 359-366. Springer Berlin, Heidelberg.

729   Weiss, Y., Griffin, W.L., Elhlou, S., and Navon, O. (2008) Comparison between LA-ICP-MS

730   and EPMA analysis of trace elements in diamonds. Chemical Geology, 252, 158–168.

731   Wieser, P., and Gleeson, M. (2023) PySulfSat: An open-source Python3 Tool for modeling

732   sulfide and sulfate saturation. Volcanica, 6, 107–127.

733   Williams, M.L., Jercinovic, M.J., and Hetherington, C.J. (2007) Microprobe Monazite

734   Geochronology: Understanding Geologic Processes by Integrating Composition and

735   Chronology. Annual Review of Earth and Planetary Sciences, 35, 137–175.

736   Wirth, R., Reid, D., and Schreiber, A. (2013) Nanometer-sized platinum-group minerals (PGM)

737   in base metal sulfides: New evidence for an orthomagmatic origin of the Merensky Reef

738   PGE ore deposit, Bushveld Complex, South Africa. The Canadian Mineralogist, 51, 143–

739   155.

740   Zhang, Z., and Hirschmann, M.M. (2016) Experimental constraints on mantle sulfide melting up

741   to 8 GPa. American Mineralogist, 101, 181–192.

742   Zhang, Z., Dorfman, S.M., Labidi, J., Zhang, S., Li, M., Manga, M., Stixrude, L., McDonough,

743   W.F., and Williams, Q. (2016) Primordial metallic melt in the deep mantle. Geophysical

744   Research Letters, 43, 3693–3699.

745

746   **Figure Captions**

747   **Figure 1.** Backscattered electron images of our experiments. A) Low-S experiment T124, with

748   0.1 wt.% bulk S, was conducted at 1.5 GPa and 1200 °C and yielded two phases: silicate glass

749   and clinopyroxene. B) High-S experiment T168, with 6.08 wt.% bulk S, was conducted at 3.0

750   GPa and 1300 °C and yielded four phases: glass, sulfide, clinopyroxene, and garnet. Some

751 clinopyroxene inclusions can be seen in the garnets. <20 μm sulfide blebs are densely

752 distributed, both throughout the glass and among silicate mineral grains.

753

754 **Figure 2.** Sulfur peak scans at a) 50, b) 100, c) 150, and d) 200 nA beam currents, collected on

755 the PETH crystal. Increased current raises both the background signal and the peak signal (at

756 171.072 mm), improving the net intensity or resolution of the peak signal from the background.

757

758 **Figure 3.** Sulfur detection limit vs. counting time and beam current, as measured on the primary

759 standard NMNH 113716-1 (1200 ppm S). Beam current exerts the primary control on lowering

760 the detection limit for S.

761

762 **Figure 4.** Uncertainty in analysis vs. beam current and total counting time, as measured on a)

763 primary standard NMNH 113716-1 (1200 ppm S) and b) secondary standard FRND6001 (44

764 ppm S). Each datapoint is an average of 2-3 replicate measurements. Dashed lines represent

765 logarithmic regression fits of each counting time series. Beam current exerts the primary control

766 on lowering uncertainty, with counting time only having a secondary effect.

767

768 **Figure 5.** Intensity of S signal and absorbed current vs. elapsed counting time across peak

769 position, low background (BG-), and high background (BG+), measured for low-S secondary

770 standards a) T120 (183 ppm S) and b) FRND6001 (44 ppm S). Despite a high beam current of

771 200 nA and extended peak counting time of 120 seconds, the intensity of the S peak remains

772 constant, indicating no volatile loss by irradiation. In a) the S peak is clearly resolved from the

773 background for T120, but in b) the peak of the more dilute FRND6001 is not clearly resolved

34

774   from the low background due to either overlap with the Fe Kβ_5 peak or background asymmetry

775   arising from spectrometer geometry.

776

777   **Figure 6.** Reproduction of primary and secondary standard measurements using EPMA. All

778   standards are reproduced to within error of reported values (Table 3). Of particular note is the 44

779   ppm S standard FRND6001, measured as 36 ± 13 ppm, demonstrating reproducibility of low S

780   contents within one standard deviation.

781

782   **Figure 7.** Sulfur peak position on primary standard NMNH 113716-1 (1200 ppm), a) before

783   extended beam exposure, and b) after >260 seconds of irradiation. The central peak position at

784   172.065 mm remains unchanged, despite some fluctuation in the peak shape that is of

785   comparable magnitude to background continuum fluctuations. Pyrite (S^{2-}) was calibrated to

786   172.122 mm in this session.

787

788   **Figure 8.** Normalized frequency distribution of sulfur concentrations measured in replicate

789   analyses of clinopyroxene in low-S experiment T124. 65% of all measurements fall below the 17

790   ppm detection limit, while 15% are considered to be high outliers that likely reflect the

791   incorporation of a subsurface S-rich heterogeneities in the analytical volume. When these

792   datapoints are discarded from calculations, only 20% of replicate measurements are considered

793   viable. Therefore, we could only bracket an upper limit of the average S contents of nominally S-

794   free minerals for the low-S bulk composition.

795

796   **Figure 9.** Sulfur contents of experimental clinopyroxene (cpx) and garnet (gt) in this study and

797   cpx from Callegaro et al. (2020), both at sulfide-saturated (closed symbols) and sulfide-

798   undersaturated (open symbols) conditions, plotted against the calculated mineral-melt partition

799   coefficients of S ($D_s^{mineral/melt}$). The mineral S and $D_s^{cpx/melt}$ of our sulfide-undersaturated

800   experiment represent upper limits calculated from highly heterogeneous replicate measurements

801   in minerals (Fig. 8), as indicated by the arrows pointing left and down. Values for our sulfide-

802   saturated silicate minerals are within error of the corresponding Callegaro et al. (2020) values,

803   suggesting apparent consistency of S capacity despite differing experimental conditions, and

804   consistency between EPMA and SXRF measurements. However, it remains uncertain whether

805   the higher mineral S contents in our high bulk-S experiments are owing to structurally-bound S,

806   or variable proportions of sulfide micro- to nano-inclusions; therefore, these may also be

807   maximum bounds on S capacity and $D_s^{mineral/melt}$, as indicated by arrows and question marks.

808

809   **Tables**

810   **Table 1.** Composition of basaltic glass standards

Standard	SiO_2	TiO_2	Al_2O_3	FeO^T	MnO	MgO	CaO	Na_2O	K_2O	P_2O_5	S (ppm)
G669	54.68(21)	2.15(9)	13.82(11)	12.21(25)	0.19(3)	3.70(8)	7.27(9)	3.11(8)	1.85(4)	0.37(2)	1560(100)
NMNH 113716-1	51.52(112)	1.3	15.39(100)	9.24(94)	0.17	8.21(101)	11.31(83)	2.48(125)	0.09	0.12	1200
B503	55.55(70)	2.14(5)	13.84(20)	11.78(15)	0.19(4)	3.82(8)	6.90(10)	2.68(52)	1.78(6)	0.33(4)	600(40)
B502	55.55(68)	2.21(10)	13.30(15)	11.99(21)	0.18(3)	3.64(15)	7.05(13)	3.02(16)	1.75(4)	0.33(2)	300(30)
T120	55.38(40)	2.19(6)	12.87(15)	12.15(34)	0.19(2)	3.65(28)	7.03(12)	3.20(7)	1.79(4)	0.35(1)	180(20)
FRND6001	55.06(9)	0.46(2)	13.33(1)	8.60(4)	0.14(1)	6.37(9)	11.23(7)	1.61(4)	0.45(1)	0.09(2)	44(1)

811   Major oxides are in weight percent, while sulfur content is given in ppm by weight. FeO^T

812   indicates total iron content. Uncertainties are given as 1σ where available, with the last

813   significant digit(s) reported in parentheses. For example, 54.68(21) should be read as 54.68 ±

814   0.21 ppm. NMNH 113716-1 is as reported by Smithsonian (National Museum of Natural

815   History, 2019), measured by Jarosewich et al. (1980) using "classical methods" for major

816   elements (uncertainty only provided where available), while in-house secondary standards G669,

817   B503, B502, and T120 are as measured using EPMA, and FRND6001 is as measured by Lloyd

818   et al. (2013) using EPMA for major elements and SIMS for sulfur.

819

820   **Table 2.** Experimental starting compositions

	SiO_2	TiO_2	Al_2O_3	FeO^T	MnO	MgO	CaO	Na_2O	K_2O	S	Total	H_2O
HAB1	47.87	0.75	17.95	9.82	0.20	5.99	10.97	2.00	0.50	0.10	96.14	3.86
HAB2	39.96	0.62	14.99	18.71	0.17	5.00	9.16	1.67	0.42	6.08	96.78	3.22

821   All values are reported in weight percent, as weighed during mixing. FeO^T indicates total Fe

822   content. Sulfur was introduced to HAB1 as pyrite (FeS_2) powder, and to HAB2 as reagent-grade

823   FeS powder. H_2O content is calculated as the deficiency from the sum of oxides.

824

825   **Table 3.** Major element oxide and sulfur concentrations of standards measured using EPMA

Standard	N	SiO_2	TiO_2	Al_2O_3	FeO^T	MnO	MgO	CaO	Na_2O	K_2O	S (ppm)	Total
G669	18	54.61(48)	2.14(6)	13.56(45)	12.06(21)	0.18(2)	3.52(9)	7.04(13)	3.15(5)	2.06(22)	1482(46)	98.32
NMNH 113716-1	20	51.61(31)	1.30(4)	15.39(42)	8.91(33)	0.17(1)	8.19(17)	11.43(17)	2.58(9)	0.08(1)	1193(52)	99.66
B503	21	54.58(53)	2.19(3)	13.29(42)	12.06(16)	0.19(1)	3.63(10)	7.02(7)	3.08(5)	1.90(5)	611(32)	97.95
B502	14	54.91(40)	2.19(8)	13.65(65)	11.92(34)	0.19(1)	3.57(9)	7.06(6)	3.17(6)	2.20(20)	253(28)	98.86
T120	21	54.17(20)	2.17(3)	13.04(35)	11.80(44)	0.19(1)	4.23(34)	6.94(17)	3.09(4)	1.99(12)	151(19)	97.63
FRND6001	20	53.38(18)	0.43(2)	15.47(25)	8.12(9)	0.15(1)	6.54(30)	10.92(8)	1.37(4)	0.50(6)	36(13)	96.88
San Carlos olivine	47	40.89(28)	BDL-	0.04(1)	9.70(7)	0.14(1)	48.26(50)	0.09(1)	0.01(0)	BDL-	17(5)	99.13

826   Major oxides are in weight percent, while S content is given in ppm by weight. FeO^T indicates

827   total Fe content. Uncertainties are given as 1σ where available, with the last significant digit(s)

828   reported in parentheses. For example, 54.61 ± 0.48 wt.% is reported as 54.61(48). Sulfur

829   concentrations are reported with the San Carlos olivine S value of 17 ± 5 ppm subtracted and the

830   uncertainty propagated.

831

832   **Table 4.** Compositions of experimental phases determined using EPMA

37

| Run#	P (GPa)	T (°C)	Phase	n	SiO_2	TiO_2	Al_2O_3	FeO^T	MnO	MgO	CaO	Na_2O	K_2O	Total	Melt H_2O	S (ppm)	$D_S^{min/melt}$	Model SCSS (ppm)
T124	1.5	1200	gl	15	52.47(24)	0.85(2)	18.23(8)	8.58(9)	0.19(5)	4.77(5)	10.25(9)	2.19(7)	0.50(2)	98.23	1.77	802(20)		--
			cpx	4	49.70(42)	0.42(4)	10.04(30)	7.51(22)	0.21(1)	12.43(43)	18.23(63)	0.63(5)	0.04(4)	99.23		62(24)	0.077(30)	
T131	1.5	1200	gl	5	52.49(23)	0.81(5)	17.94(5)	6.92(9)	0.16(1)	5.00(5)	10.06(10)	2.37(7)	0.60(2)	96.54	3.46	775(71)		740(202)
			cpx	15	50.53(47)	0.30(4)	7.87(91)	7.74(54)	0.18(1)	14.38(52)	18.95(39)	0.62(4)	0.00(1)	100.59		71(35)	0.092(46)	
T154	2.5	1250	gl	14	53.45(100)	0.89(4)	14.91(54)	8.59(41)	0.10(2)	3.09(27)	9.36(72)	1.66(48)	0.64(8)	92.86	7.14	742(132)		681(186)
			cpx	19	52.81(56)	0.23(2)	6.90(25)	7.86(15)	0.09(2)	10.15(19)	19.11(15)	1.89(7)	BDL-	99.05		38(17)	0.052(25)	
			gt	15	42.51(45)	0.30(4)	21.04(46)	17.04(36)	0.40(2)	8.77(18)	9.91(29)	0.05(6)	0.00(1)	100.04		63(28)	0.085(41)	
T155	3.0	1250	gl	10	57.15(163)	0.99(5)	14.44(36)	6.64(52)	0.08(1)	2.19(22)	8.00(73)	1.21(44)	0.87(9)	91.69	8.31	447(189)		572(156)
			cpx	12	53.01(38)	0.27(3)	7.47(26)	7.81(11)	0.07(1)	9.03(14)	18.00(13)	2.84(6)	0.01(1)	98.53		43(22)	0.095(64)	
			gt	14	41.24(43)	0.39(6)	20.90(49)	17.83(34)	0.37(2)	7.66(25)	10.93(26)	0.09(7)	BDL -	99.42		49(20)	0.110(64)	
T168	3.0	1300	gl	12	57.85(53)	1.00(2)	16.35(27)	4.29(17)	0.10(1)	2.72(6)	9.71(10)	2.30(7)	0.69(1)	95.15	4.85	634(75)		903(246)
			cpx	10	51.26(55)	0.41(2)	14.28(61)	3.42(48)	0.13(1)	9.79(44)	18.51(16)	2.17(8)	BDL-	99.97		44(24)	0.070(39)	
			gt	12	41.76(36)	0.35(4)	22.68(29)	10.84(43)	0.58(3)	13.19(44)	11.24(23)	0.05(5)	BDL-	100.70		47(28)	0.075(45)	

833   Major oxides are in weight percent, while S content is given in ppm by weight. FeO^T indicates

834   total Fe content. Uncertainties are given as 1σ where available, with the last significant digit(s)

835   reported in parentheses. For example, 52.47 ± 0.24 wt.% is reported as 52.47(24). Sulfur

836   concentrations are reported with the San Carlos olivine S value of 17 ± 5 ppm subtracted and the

837   uncertainty propagated. Experiment T124 uses low-S starting mix HAB1 and is sulfide-

838   undersaturated, while T131, T154, T155, and T168 are sulfide-saturated, using high-S starting

839   mix HAB2. 15 spots were set for all glass phases and 20 for minerals, with n representing the

840   actual number of replicate analyses used to calculate mean composition once anomalously high

841   and below the D.L. values of sulfur were omitted. Melt H_2O (wt.%) is calculated as the deficit in

842   total cations, to add up to a sum of 100%. Model SCSS is calculated with the Smythe et al.

843   (2017) model, using the PySulfSat program (Wieser and Gleeson, 2023).

844

845   **Figures**
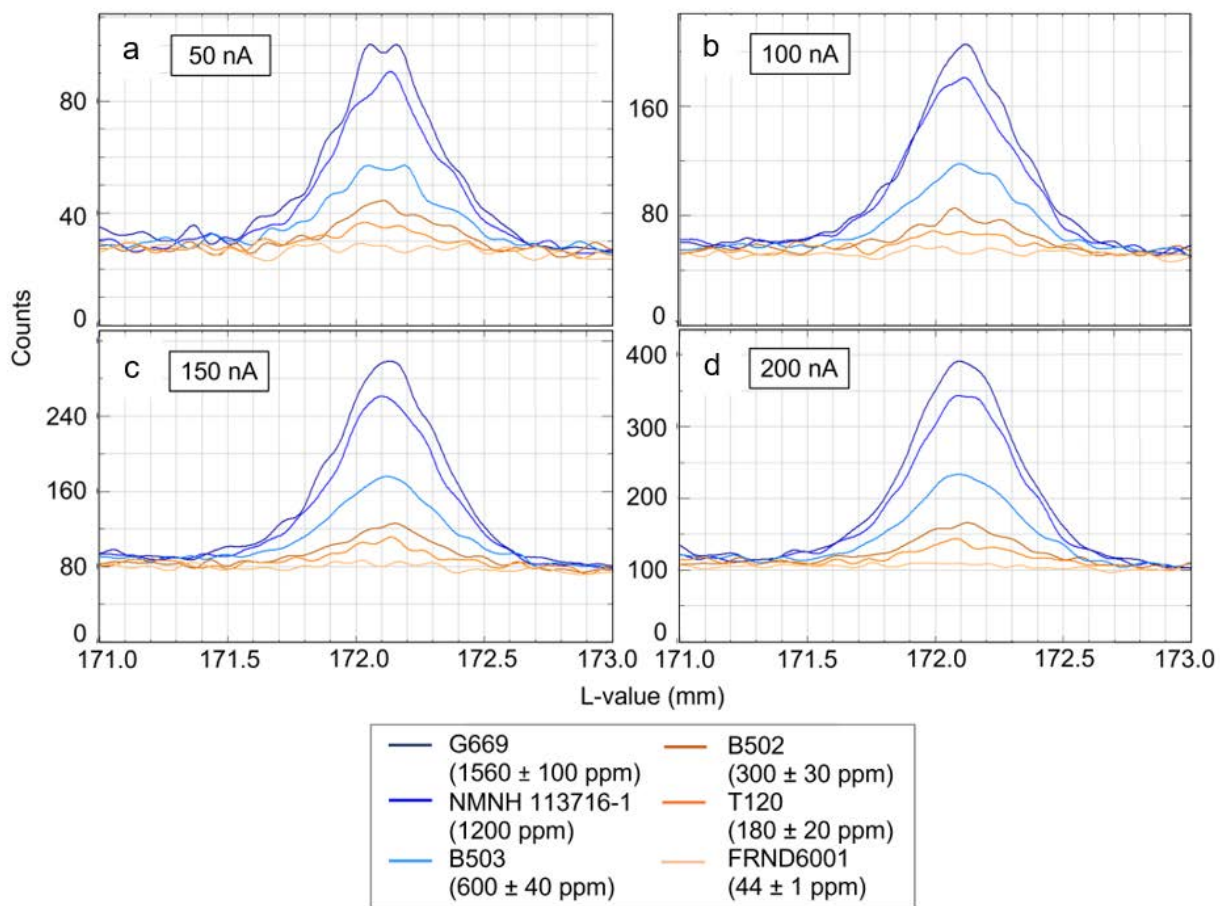
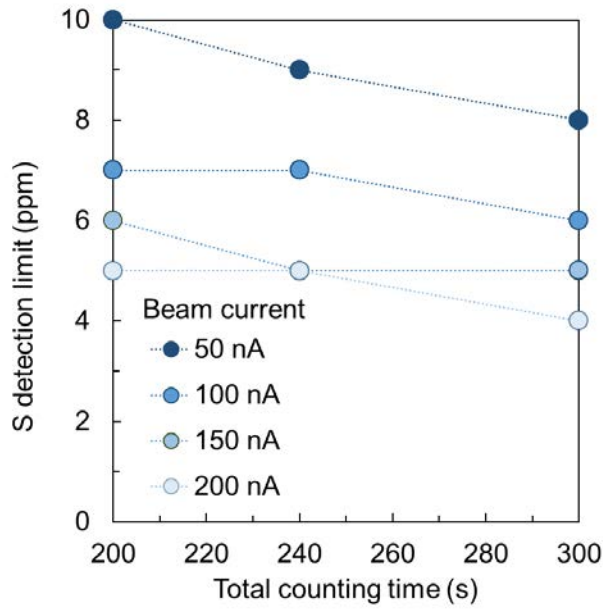846 **Figure 1**
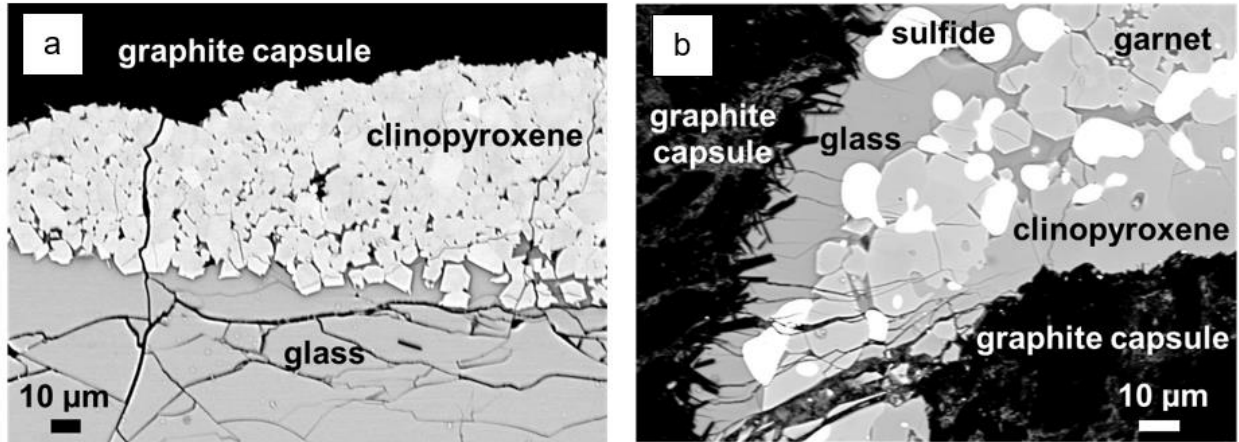
847

848

849 **Figure 2**

850

851
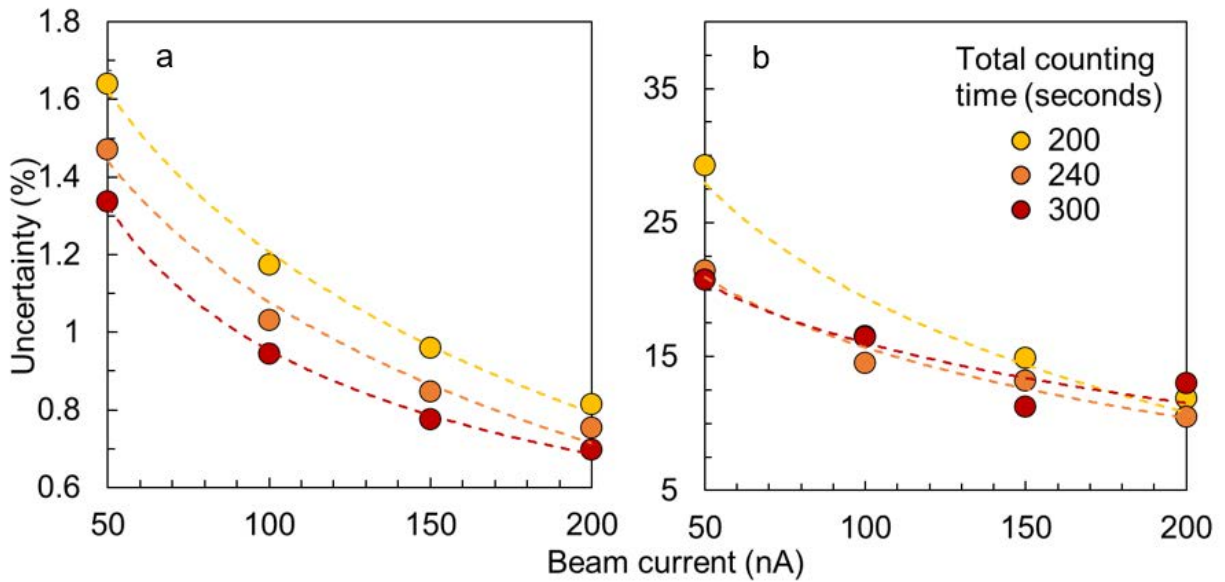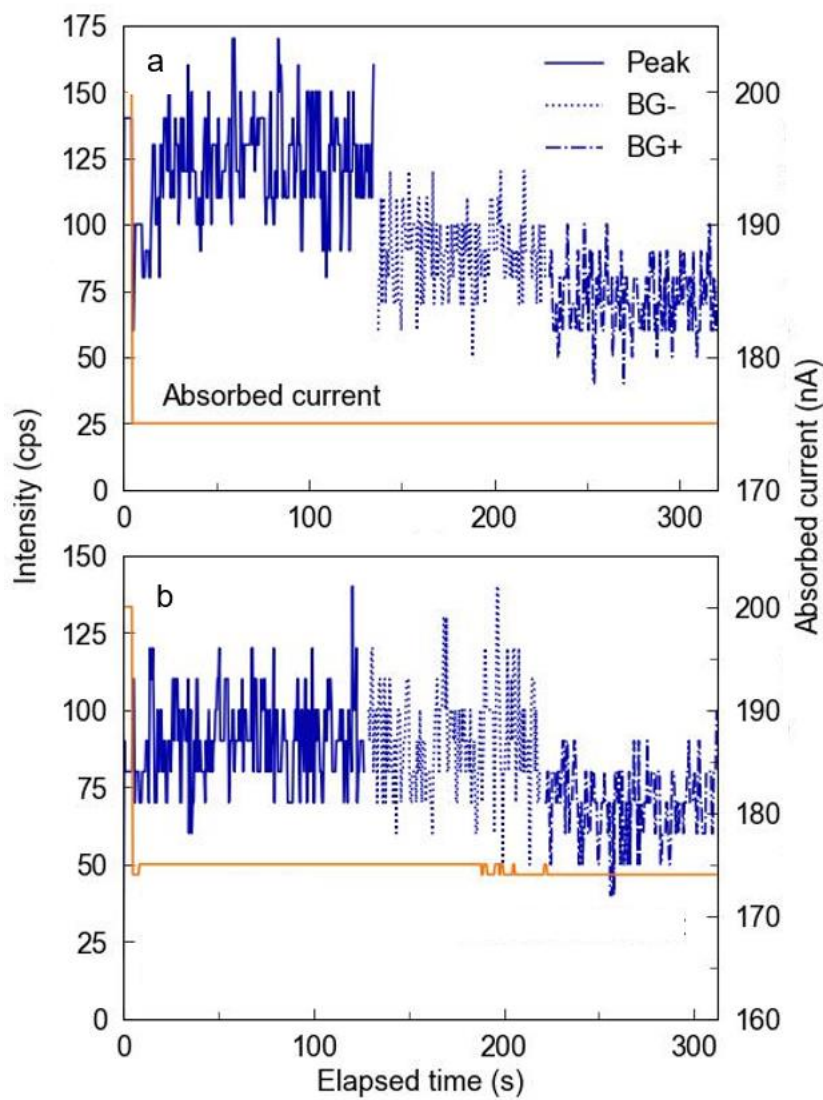
852 **Figure 3**
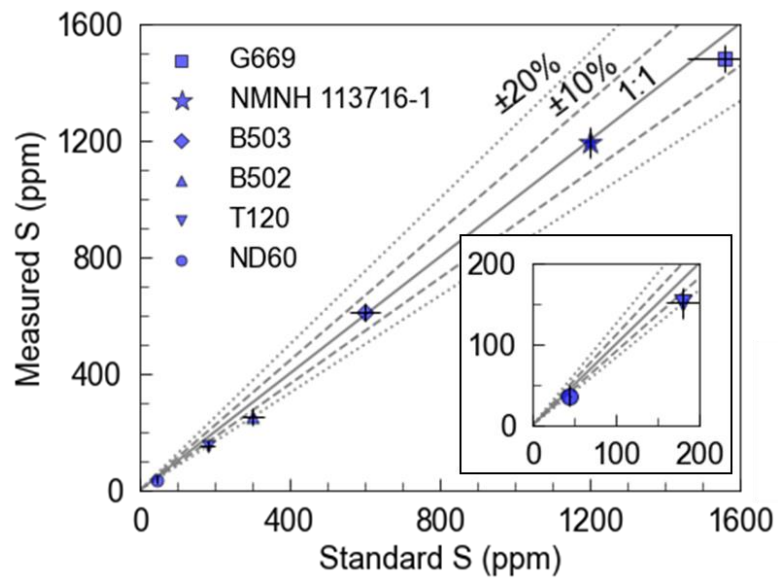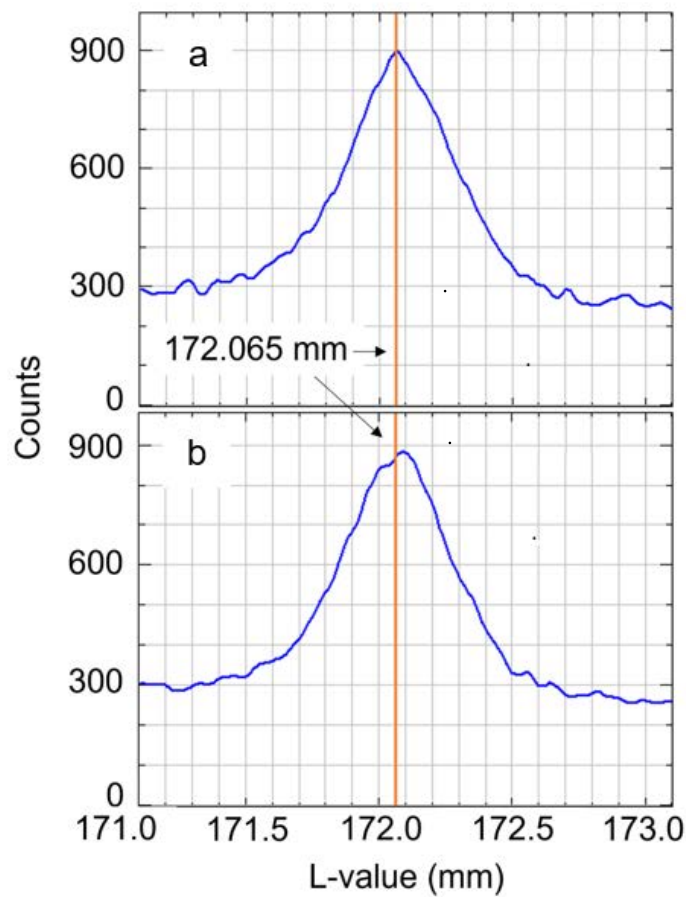
853

854

855   **Figure 4**
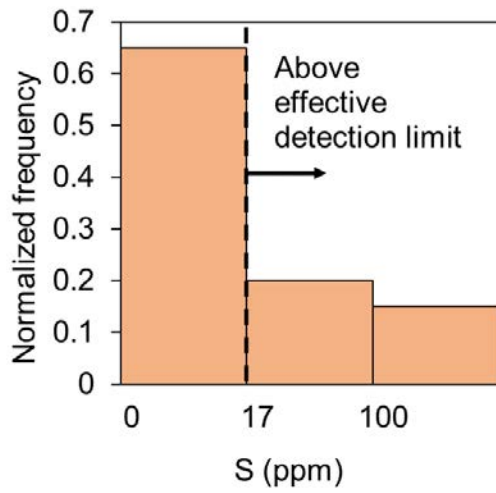

856

857

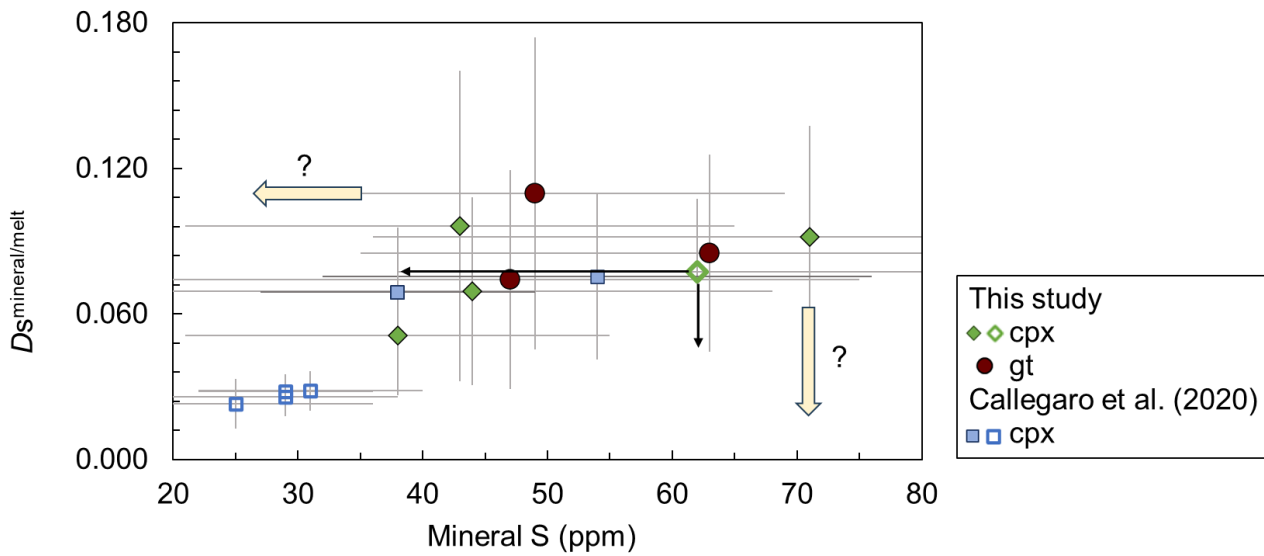858   **Figure 5**

859

860
861   **Figure 6**

42

862

863   **Figure 7**

864

865

43

866 **Figure 8**

867

868 **Figure 9**

869

44